International Journal of Coal Geology 156 (2016) 36–49

Contents lists available at ScienceDirect

International Journal of Coal Geology

journal homepage: www.elsevier.com/locate/ijcoalgeo

Characterization of methane adsorption on overmature Lower Silurian–Upper Ordovician shales in Sichuan Basin, southwest China: Experimental results and geological implications

Hui Tian [a,b], Tengfei Li [a], Tongwei Zhang [b,*], Xianming Xiao [a,**]

[a] State Key Laboratory of Organic Geochemistry, Guangzhou Institute of Geochemistry, Chinese Academy of Sciences, Guangzhou 510640, China
[b] Bureau of Economic Geology, University of Texas at Austin, Austin, TX 78758, United States

ARTICLE INFO

Article history:
Received 13 August 2015
Received in revised form 29 January 2016
Accepted 31 January 2016
Available online 2 February 2016

Keywords:
Shale gas
Methane adsorption
Gas-in-place
Sichuan Basin

ABSTRACT

A series of methane adsorption isotherms were measured at 35.4 °C, 50.6 °C, and 65.4 °C at pressures up to 15.0 MPa for eight dried, overmature Lower Silurian–Upper Ordovician shale samples collected from the Sichuan Basin with TOC values in the range of 1.87–5.74%. The measured maxima of excess adsorption capacity of methane range from 1.25 to 2.50 cm^3/g rock at 65.4 °C; the maxima are slightly enhanced at 35.4 °C, but all are positively correlated with total organic carbon (TOC). Both the supercritical Dubinin–Radushkevich (SDR)- and Langmuir-based excess adsorption models were found to represent the experimental excess adsorption isotherms equally well within the experimental range. The temperature-dependent densities of adsorbed methane resulting from the parameter fit of the SDR-based excess adsorption model are in the range of 297–415 mg/cm^3; for the Langmuir-based excess adsorption model, the adjusted densities range from 386 mg/cm^3 to 1027 mg/cm^3 and most of them are much larger than the liquid density of methane at its boiling point (424 mg/cm^3). Nevertheless, the maxima of absolute methane adsorption capacity fitted by both models are not significantly different and are linearly correlated. One of the contributors to the uncertainty of the gas-in-place estimation in geological conditions is the inconsistent utilization of experimental excess sorption data as "absolute sorption" values, particularly at high pressures. However, the choice of adsorption model itself (Langmuir- or SDR-based) and the fitting procedure, assuming either constant or temperature-dependent adsorbed phase density and maximum sorption capacity, do not significantly affect the estimated GIPs for the geological system studied here with depths of less than 4000 m.

1. Introduction

Gas-in-place (GIP) is a key parameter for the economic evaluation of a shale reservoir. The gas in shale reservoirs can be stored as free gas in pores and fractures, adsorbed gas on various surfaces, and absorbed gas dissolved in any liquids (Curtis, 2002). For shale reservoirs bearing liquid petroleum, it is difficult to determine precisely the disposition of adsorbed and absorbed gas, so they are generally referred to as sorbed gas (Montgomery et al., 2005). For overmature shale reservoirs, e.g., the Lower Silurian to Upper Ordovician shales in the Sichuan Basin, the gas dissolved in liquid petroleum could be neglected because the retained liquid petroleum in shale reservoirs has been totally cracked to gas.

The contribution of adsorbed gas to GIP varies significantly among shales. For example, the sorbed gas accounts for only about 20% of original gas-in-place (OGIP) in the Barnett shale-gas system, but it is as high as 60–85% in the Lewis shale-gas system (Curtis, 2002). Unlike free gas storage capacity that is principally controlled by porosity, temperature, pressure, and gas saturation, the gas storage resulting from physical sorption is a complex function of chemical and pore-structural characteristics of the rock matrix, the properties of fluid phases, and reservoir temperature and pressure (Chalmers and Bustin, 2008; Gasparik et al., 2012; Rexer et al., 2013). Previous studies have shown that organic matter is a main contributor to sorptive gas storage capacity, and positive relationships were established between the total organic carbon (TOC) and adsorbed gas capacity (Ross and Bustin, 2009; Weniger et al., 2010; Zhang et al., 2012; Gasparik et al., 2014a; Ji et al., 2014).

In some cases, clay minerals can also contribute significantly to adsorbed gas capacity when they are dominated by a montmorillonite and I–S mixed layer that has much larger methane adsorption capacities than illite and chlorite minerals (Gasparik et al., 2012; Ji et al., 2012). The adsorption capacity of shales or coals, however, may be reduced substantially when water is present in the sample because water may occupy adsorption sites and block the pore

* Correspondence to: T. Zhang, 10100 Burnet Road, Austin, TX 78758, United States.
** Correspondence to: X. Xiao, #511 Kehua Road, Tianhe District, Guangzhou City, Guangdong Province, China.
E-mail addresses: tongwei.zhang@beg.utexas.edu (T. Zhang), xmxiao@gig.ac.cn (X. Xiao).

http://dx.doi.org/10.1016/j.coal.2016.01.013
0166-5162/

system. Both processes adversely affect the methane adsorption capacity (Krooss et al., 2002; Chalmers and Bustin, 2008; Busch and Gensterblum, 2011; Gasparik et al., 2014a; Gensterblum et al., 2014a).

The experimental excess adsorption of methane can be parameterized and extrapolated to geological conditions by various models, including Langmuir, supercritical Dubinin–Radushkevich (SDR), and simplified local density (SLD) models (Chareonsuppanimit et al., 2012; Gasparik et al., 2012; Clarkson and Haghshenas, 2013; Rexer et al., 2013). Fitted parameters such as density or volume of the adsorbed gas phase can be used to derive "absolute" adsorption isotherms from the experimentally measured excess adsorption isotherms. The absolute adsorption isotherms at various temperatures can be utilized to estimate the thermodynamic parameters of methane adsorption, such as adsorption heat and entropy (Zhang et al., 2012; Rexer et al., 2013; Gasparik et al., 2014a; Hu et al., 2015).

Shale gas evaluation and exploration in China are mainly focused around South China, where the Paleozoic black marine shales are widely developed (Zou et al., 2010; Tan et al., 2014a, 2014b). These black shales are good-to-excellent source rocks and have sourced the conventional petroleum systems in and around the Sichuan Basin today (Zou et al., 2010). Abundant pyrobitumen is observed in both the Lower Silurian–Upper Ordovician and Lower Cambrian black shales (Tian et al., 2013, 2015), which indicates that parts of liquid oils were retained after their primary migration and further cracked to gaseous hydrocarbons following deep burial. These oil-cracking gases, along with the gases from the cracking of residual kerogen, are the main source of shale gas (Hill et al., 2007; Jarvie et al., 2007; Strąpoć et al., 2010; Xia et al., 2013).

In recent years, significant progress on shale gas has been achieved in Lower Silurian–Upper Ordovician shales within and around the Sichuan Basin (EIA, 2013; Guo and Zhang, 2014). Many studies on these shales have revealed that they are qualified as shale reservoirs and can be compared to North American shales with respect to their TOC, mineralogical composition, porosity, and pore size (Chen et al., 2011; Long et al., 2012; Tian et al., 2013; Tan et al., 2014b; Wang et al., 2014). However, the characterization and capacity of methane adsorption of these shales are still poorly studied and documented (Wang et al., 2013; Tan et al., 2014a; Ma et al., 2015). Therefore, the present study collected eight core samples from Lower Silurian–Upper Ordovician shales in the southeastern Chongqing area, near the eastern Sichuan Basin, and performed methane adsorption experiments at 35.4 °C, 50.6 °C, and 65.4 °C at pressures up to 15.0 MPa. The objectives of this study are to (1) investigate the methane adsorption capacity and characteristics of Lower Silurian–Upper Ordovician shales, and (2) discuss the controls on methane adsorption and its implication to the evaluation of GIP in the studied area.

2. Samples and methods

2.1. Samples and geological settings

Eight core samples were collected from the YC4 well in the southeastern Chongqing area, which is near the producing Jiaoshiba shale gas play in eastern Sichuan Basin (Fig. 1). The sampling depth ranges from 648.2 to 760.9 m and covers six Lower Silurian and two Upper Ordovician black shale samples (Table 1). The Sichuan Basin is a remnant of the originally much larger Upper Yangtze cratonic sedimentary basin; the southeastern Chongqing area was separated from the present Sichuan Basin after several tectonic collisions that have occurred since the Late Triassic (Zeng et al., 2012). The Wufeng Formation of the Upper Ordovician was formed in the depositional environments of the deep-water continental shelf, which was inherited by the Longmaxi Formation of the Lower Silurian that overlies the Wufeng Formation without unconformity (Zou et al., 2010).

2.2. TOC, thermal maturity, and minerals

Total organic carbon (TOC) of the samples was measured by a LECO CS-200 analyzer after treatment with hydrochloric acid to remove carbonates. Because of the lack of vitrinite in the sampled shales, the reflectance of pyrobitumen was measured on polished blocks using a 3Y microphotometric system. The random reflectance was measured in oil immersion ($n = 1.518$) at 546 nm using a 50×/0.85 objective lens.

X-ray diffraction (XRD) analysis of shale powders was carried out on a Bruker D8 ADVANCE X-ray diffractometer at 40 kV and 30 mA with a Cu Kα radiation ($\lambda = 1.5406$ for CuKα1). Stepwise scanning measurements were performed at a rate of 4°/min in the range of 3–85° (2θ). The relative mineral percentages were estimated semi-quantitatively using the area under the curve for the major peaks of each mineral, with correction for Lorentz Polarization (Chalmers and Bustin, 2008).

2.3. Low-pressure nitrogen gas adsorption

The N_2 adsorption at 77.4 K was carried out on a Micromeritics ASAP 2020^M apparatus. The shale samples were manually crushed and sieved into grains of about 20–50 mesh size (300–750 μm), dried in a vacuum oven at 110 °C overnight, and degassed in the apparatus under high vacuum (<10 mm Hg) for 12 h at 110 °C to further remove adsorbed moisture and volatile matter. The relative pressure (p/p_0) for N_2 adsorption ranges from 0.0009 to 0.995. Both adsorption and desorption isotherms were measured to investigate the hysteresis types of N_2 adsorption. The Brunauer–Emmett–Teller (BET), Barrett–Joyner–Halenda (BJH), and Dubinin–Radushkevich (DR) equations were applied to N_2 adsorption isotherms to derive the total specific surface area, non-micropore surface area, and micropore surface area and volume (Sing et al., 1985).

2.4. Methane adsorption

2.4.1. Methane excess adsorption

Adsorption isotherms with methane were measured at 35.4 °C, 50.4 °C, and 65.4 °C at pressures ranging from 0.2 to 15.0 MPa in the Geochemistry Lab of the Bureau of Economic Geology, University of Texas at Austin. The measurements were conducted on a setup built on the basis of the manometric method that has been documented in the literature (Krooss et al., 2002; Gasparik et al., 2012; Zhang et al., 2012; Hu et al., 2015). For our study, the main procedures include: (1) sample pretreatment. The same grain fractions as used in the low-pressure nitrogen adsorption experiment are dried at 110 °C for about 24 h under a helium flow rate of about 5 cm^3/min to remove the moisture in the sample; (2) leak test. After loading about 6–7 g of dry sample into the sample cell, the whole system was evacuated at experimental temperatures. Then both reference and sample cells were pressurized with He gas up to 15 MPa for a leak test at a constant temperature. The accepted leakage is less than 6.89×10^{-4} MPa/h (0.1 psi/h); (3) void volume determination. The void volume of the loaded sample cell was determined by helium expansion at 35.4 °C, 50.4 °C and 65.4 °C individually and applied in the calculation of corresponding methane adsorption isotherms. This procedure was found to be appropriate to correct the systematic error in void volume caused by changing the system temperature (Gasparik et al., 2015; Hu et al., 2015); (4) methane adsorption. A certain amount of methane was transferred to the reference cell, and after the gas pressure in the reference cell had become constant, the valve connecting reference and sample cells were opened, and the pressure between the two cells was allowed to equilibrate. When pressure changes were less than 6.89×10^{-4} MPa (0.1 psi) in 20 min, the adsorption equilibrium was assumed to be achieved. Then the excess adsorption of methane at a given temperature was calculated using the routine methods

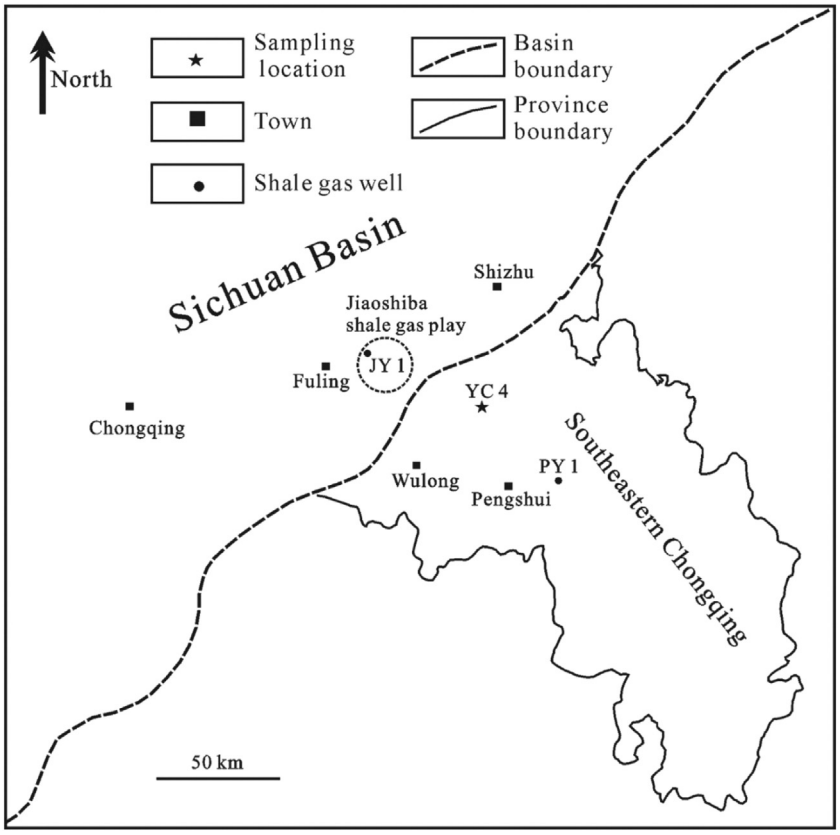

Fig. 1. Schematic map showing sampling location (modified from Guo and Zhang (2014)).

reported in the literature (Krooss et al., 2002; Zhang et al., 2012; Gasparik et al., 2012, 2014a). The uncertainty of calculated excess adsorption increases with pressure and varies among samples under different temperatures (Gasparik et al., 2012, 2014b). The maximum error derived from the uncertainty of the void volume is estimated to be about 0.2 cm^3/g rock at 15 MPa when reported under STP conditions (temperature = 0 °C and pressure = 0.1 MPa), close to that reported by Gasparik et al. (2012).

2.4.2. Calculation of absolute methane adsorption

The measured excess adsorption (n_{excess}) and the absolute adsorption (n_{abs}) are related according to Eqs. (1) and (2). The transformation of excess adsorption to absolute adsorption therefore requires a value for either the density (ρ_{ads}) or volume (V_{ads}) of adsorbed methane (Krooss et al., 2002; Gasparik et al., 2012; Rexer et al., 2013). These equations indicate that the difference between "excess" and "absolute" adsorption only becomes remarkable at high pressures, although it is always there at low pressures.

$$n_{excess} = n_{abs} \cdot \left(1 - \frac{\rho_g}{\rho_{ads}}\right) \quad (1)$$

or

$$n_{excess} = n_{abs} - \rho_g \cdot V_{ads} \cdot C_{STP}. \quad (2)$$

Here ρ_g is the density of free methane at a given temperature and pressure and C_{STP} is the coefficient of a unit conversion from mass to volume under STP conditions and equal to 1.4 cm^3/mg for methane. The methane density was calculated according to the high-accuracy equation of state (EoS) of Setzmann et al. (1991). Density values calculated with this EoS are available at the website of the U.S. National Institute of Standards and Technology (NIST).

Table 1
Basic geological and geochemical parameters of our eight shale samples.

Sample	Age	Depth (m)	TOC (%)	Pyrobitumen reflectance (%)	XRD mineralogical composition (%)							S_{BET}[a]	S_{BJH}[a]	S_{DR}[a]	V_{DR}[a]
					Quartz	Feldspar	Carbonates	Pyrite	Illite	Chlorite	Total clays	m^2/g	m^2/g	m^2/g	cm^3/kg
YC4-04	S_1	648.2	1.87	nd	25.4	9.6	9.9	nd	31.5	23.5	55.0	12.5	5.5	6.6	4.7
YC4-08	S_1	657.2	2.45	nd	32.5	11.5	3.2	1.7	36.5	14.6	51.1	16.9	7.0	9.0	6.4
YC4-33	S_1	705.4	1.99	nd	24.4	15.0	nd	1.0	36.5	23.2	59.7	14.2	6.0	7.6	5.4
YC4-47	S_1	726.5	3.34	2.64–3.55	24.6	10.6	7.0	4.9	31.4	21.6	53.0	18.5	7.9	9.9	7.1
YC4-54	S_1	741.7	4.52	3.06–3.41	36.6	15.4	6.2	1.6	26.0	14.4	40.4	20.2	8.8	10.8	7.5
YC4-61	S_1	754.9	5.44	3.28–3.62	59.0	5.2	6.1	1.6	21.0	7.1	28.1	19.3	9.2	10.1	7.1
YC4-64	O_3	760.0	4.07	3.10–3.55	58.3	8.4	nd	nd	18.2	15.1	33.3	17.8	8.6	9.1	6.6
YC4-65	O_3	760.9	5.74	3.20–3.53	56.5	9.1	nd	nd	26.1	8.3	34.4	20.6	11.8	10.4	7.6

nd: no data.

[a] S_{BET}, the total surface area by the BET equation; S_{BJH}, the surface area of meso- and macro-pores by the BJH model; S_{DR} and V_{DR}, the surface area and volume of micropores by the DR equation (Sing et al., 1985).

The absolute adsorption isotherm of methane is described by the Langmuir model, which assumes monomolecular layer adsorption on surfaces (Krooss et al., 2002; Gasparik et al., 2012; Zhang et al., 2012; Gensterblum et al., 2013).

$$n_{abs} = n_0 \cdot \frac{K_L \cdot P}{1 + K_L \cdot P} \tag{3}$$

Where n_0 represents the maximum absolute adsorption capacity at a given temperature, P is the equilibrium pressure, and K_L is the temperature-dependent Langmuir constant. The Langmuir pressure (P_L), which is the reciprocal of the Langmuir constant, represents the pressure at which the amount of adsorbed methane equals half of the maximum adsorption capacity of methane—an important parameter for evaluating the efficiency of gas desorption under reservoir pressures.

The absolute adsorption of methane can also be described by the supercritical Dubinin–Radushkevich (SDR) equation, which is based on the pore-filling mechanism (Murata et al., 2001; Sakurovs et al., 2007; Clarkson and Haghshenas, 2013; Rexer et al., 2013).

$$n_{abs} = n_0 \cdot \exp\left\{-D \cdot \left[\ln\left(\frac{\rho_{ads}}{\rho_g}\right) \cdot R \cdot T\right]^2\right\} \tag{4}$$

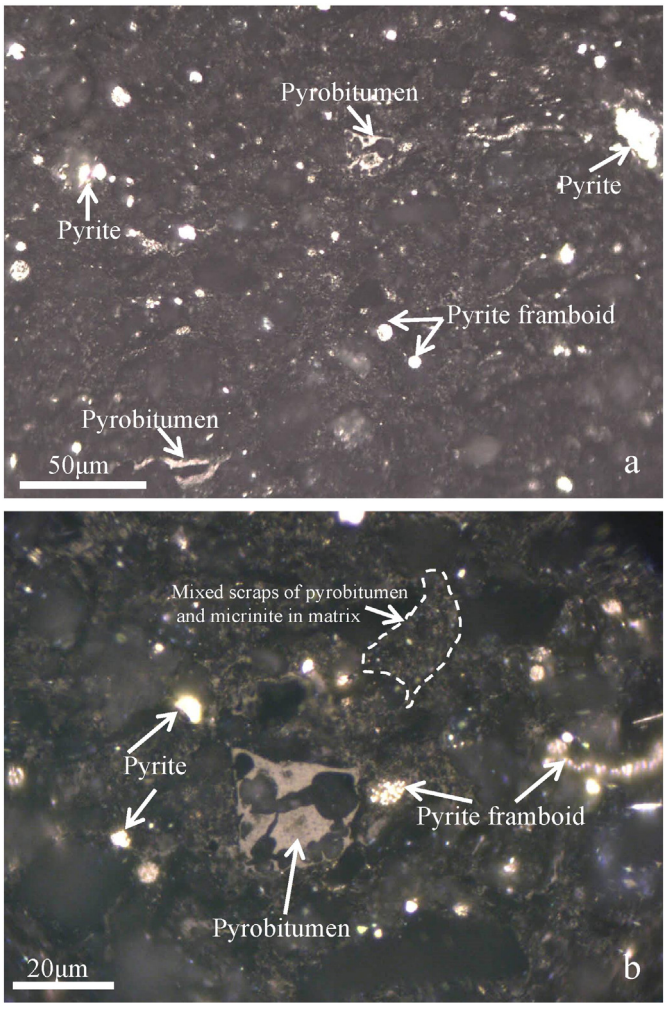

Fig. 2. Typical microphotographs of whole rock, showing pyrobitumen and micrinite macerals. The pyrobitumen is gray and occurs in shapes of both bands and scraps (a, b), but the micrinite occurs in the rock matrix and is usually mixed with pyrobitumen scraps (b). The brightest areas are the pyrite crystals and/or framboid pyrites.

Here D is a parameter related to pore structure in units of $mol^2 \cdot kJ^{-2}$, R is the ideal gas constant (8.314×10^{-3} $kJ \cdot mol^{-1} \cdot K^{-1}$), and T is the temperature in Kelvin (K).

Substituting Eq. (3) or (4) into Eq. (1),

$$n_{excess} = n_0 \cdot \frac{K_L \cdot P}{1 + K_L \cdot P} \cdot \left(1 - \frac{\rho_g}{\rho_{ads}}\right) \tag{5}$$

or

$$n_{excess} = n_0 \cdot \exp\left\{-D \cdot \left[\ln\left(\frac{\rho_{ads}}{\rho_g}\right) \cdot R \cdot T\right]^2\right\} \cdot \left(1 - \frac{\rho_g}{\rho_{ads}}\right) \tag{6}$$

Here, Eqs. (5) and (6) are referred to as the Langmuir- and SDR-based excess adsorption model, respectively. The unknown parameters in Eq. (5) include n_0, K_L, and ρ_{ads}. In Eq. 6, they are n_0, D, and ρ_{ads}. These parameters can be obtained by fitting Eqs. (5) and (6) to the three measured excess adsorption isotherms together using a least-square minimization procedure, and the fitting error (Δn) was evaluated by Eq. (7).

$$\Delta n = \frac{1}{N} \cdot \sum_i^N \left| n_i^{\exp}(p_i, T_i) - n_i^{fit}(p_i, T_i) \right| \tag{7}$$

Where $n_i^{\exp}(p_i,T_i)$ and $n_i^{fit}(p_i,T_i)$ represent respectively the measured and fitted excess adsorption amount at the ith paired temperature and

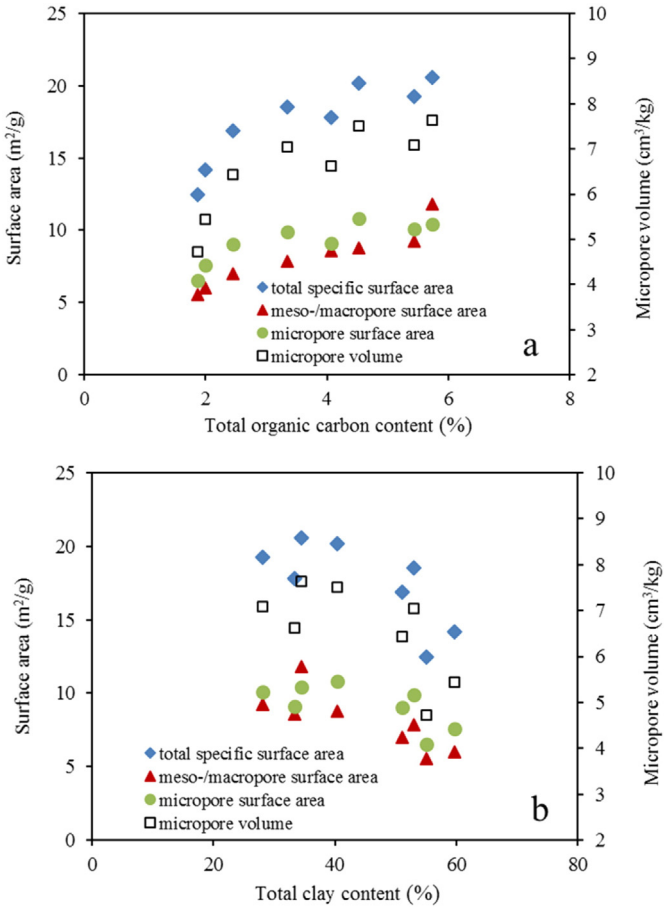

Fig. 3. Relationships of specific surface areas and micropore volumes with TOC (a) and total clay content (b) for the eight shale samples studied. Micropores are, by definition, the pores with a diameter of less than 2 nm and meso-/macro-pores are the pores with a diameter of larger than 2 nm (e.g., 2–50 nm for mesopores and >50 nm for macropores) (Sing et al., 1985).

Table 2
Measured excess adsorption of methane at different temperatures and pressures.[a]

35.4 °C		50.4 °C		65.4 °C		35.4 °C		50.4 °C		65.4 °C	
P (MPa)	CH_4 (cm^3/g rock)	P (MPa)	CH_4 (cm^3/g rock)	P (MPa)	CH_4 (cm^3/g rock)	P (MPa)	CH_4 (cm^3/g rock)	P (MPa)	CH_4 (cm^3/g rock)	P (MPa)	CH_4 (cm^3/g rock)
Sample 4–04, TOC = 1.87%						Sample 4–08, TOC = 2.45%					
0.26	0.27	0.27	0.23	0.27	0.20	0.26	0.38	0.25	0.31	0.27	0.24
0.75	0.53	0.76	0.46	0.73	0.40	0.72	0.71	0.72	0.57	0.73	0.48
1.37	0.74	1.40	0.65	1.37	0.59	1.34	0.99	1.34	0.88	1.39	0.76
2.09	0.91	2.13	0.81	2.13	0.75	2.07	1.22	2.05	1.09	2.18	0.99
2.88	1.03	2.96	0.95	3.00	0.89	2.89	1.40	2.87	1.27	3.08	1.17
3.75	1.14	3.87	1.05	3.94	1.00	3.76	1.55	3.75	1.41	4.01	1.31
4.65	1.20	4.80	1.14	4.90	1.09	4.68	1.66	4.67	1.52	4.95	1.42
5.60	1.25	5.79	1.20	5.93	1.15	5.64	1.75	5.64	1.61	5.92	1.50
6.56	1.31	6.80	1.25	6.97	1.20	6.61	1.80	6.63	1.67	6.91	1.56
7.52	1.34	7.79	1.27	8.00	1.23	7.58	1.84	7.61	1.71	7.88	1.60
8.45	1.34	8.76	1.29	9.00	1.25	8.52	1.86	8.56	1.73	8.83	1.62
9.36	1.36	9.70	1.29	9.96	1.25	9.43	1.87	9.48	1.74	9.79	1.63
10.48	1.34	10.83	1.28	11.10	1.24	10.53	1.85	10.59	1.73	10.91	1.63
11.75	1.32	12.05	1.26	12.28	1.23	11.72	1.83	11.79	1.71	12.07	1.61
12.88	1.29	13.06	1.24	13.19	1.21	12.75	1.79	12.78	1.68	12.97	1.60
13.66	1.27	13.74	1.22	13.81	1.19	13.46	1.76	13.45	1.66	13.58	1.58
14.19	1.25	14.20	1.21	14.22	1.18	13.94	1.74	13.90	1.65	14.00	1.57
Sample 4–33, TOC = 1.99%						Sample 4–47, TOC = 3.34%					
0.26	0.34	0.25	0.27	0.25	0.23	0.25	0.48	0.22	0.36	0.25	0.33
0.69	0.61	0.71	0.53	0.71	0.46	0.70	0.87	0.68	0.73	0.74	0.67
1.29	0.85	1.36	0.77	1.33	0.68	1.33	1.20	1.35	1.05	1.38	0.95
1.99	1.05	2.12	0.97	2.06	0.86	2.06	1.47	2.15	1.31	2.12	1.18
2.78	1.22	2.95	1.13	2.90	1.02	2.91	1.68	3.02	1.51	2.96	1.38
3.63	1.36	3.81	1.25	3.80	1.15	3.80	1.86	3.93	1.67	3.88	1.53
4.50	1.46	4.68	1.35	4.75	1.25	4.73	1.99	4.85	1.79	4.85	1.65
5.41	1.54	5.59	1.42	5.77	1.34	5.69	2.08	5.81	1.88	5.88	1.75
6.34	1.60	6.54	1.48	6.79	1.40	6.67	2.15	6.81	1.95	6.93	1.82
7.26	1.64	7.48	1.52	7.81	1.44	7.64	2.21	7.81	1.99	7.98	1.86
8.15	1.67	8.40	1.54	8.80	1.46	8.58	2.23	8.78	2.02	8.99	1.88
9.02	1.68	9.30	1.56	9.75	1.48	9.50	2.24	9.73	2.03	9.97	1.89
10.08	1.68	10.38	1.56	10.87	1.48	10.61	2.24	10.88	2.02	11.13	1.89
11.29	1.67	11.55	1.54	11.97	1.47	11.87	2.21	12.12	2.00	12.34	1.86
12.35	1.64	12.52	1.52	12.83	1.46	12.99	2.17	13.15	1.97	13.29	1.84
13.09	1.62	13.18	1.51	13.42	1.45	13.77	2.14	13.87	1.94	13.94	1.82
13.59	1.61	13.63	1.50	13.83	1.45	14.30	2.12	14.35	1.92	14.38	1.80
Sample 4–54, TOC = 4.52%						Sample 4–61, TOC = 5.44%					
0.18	0.52	0.17	0.39	0.19	0.34	0.19	0.59	0.20	0.51	0.21	0.44
0.54	0.99	0.53	0.82	0.56	0.70	0.61	1.15	0.62	1.02	0.64	0.90
1.06	1.37	1.07	1.20	1.08	1.02	1.17	1.57	1.24	1.44	1.26	1.29
1.66	1.67	1.72	1.50	1.71	1.29	1.83	1.89	1.98	1.77	1.96	1.59
2.35	1.92	2.48	1.75	2.43	1.52	2.59	2.15	2.78	2.02	2.75	1.83
3.09	2.11	3.25	1.93	3.20	1.71	3.41	2.35	3.62	2.21	3.59	2.02
3.85	2.26	4.02	2.08	4.00	1.86	4.26	2.51	4.47	2.35	4.47	2.17
4.66	2.38	4.82	2.19	4.85	1.98	5.15	2.63	5.36	2.46	5.41	2.29
5.47	2.47	5.63	2.28	5.71	2.07	6.06	2.72	6.28	2.54	6.37	2.37
6.29	2.53	6.44	2.34	6.57	2.15	6.96	2.78	7.20	2.60	7.33	2.43
7.08	2.58	7.24	2.39	7.40	2.20	7.84	2.82	8.10	2.63	8.26	2.47
7.85	2.60	8.04	2.42	8.20	2.24	8.69	2.84	8.97	2.65	9.16	2.49
8.78	2.62	8.99	2.44	9.14	2.27	9.73	2.84	10.02	2.65	10.23	2.50
9.78	2.62	10.02	2.45	10.13	2.29	10.91	2.82	11.17	2.62	11.34	2.48
10.63	2.61	10.85	2.44	10.90	2.29	11.95	2.79	12.12	2.60	12.22	2.46
11.21	2.60	11.42	2.43	11.42	2.29	12.68	2.76	12.77	2.58	12.82	2.45
11.60	2.60	11.79	2.42	11.77	2.29	13.17	2.74	13.21	2.56	13.23	2.44
Sample 4–64, TOC = 4.07%						Sample 4–65, TOC = 5.74%					
0.23	0.55	0.27	0.51	0.28	0.42	0.22	0.64	0.23	0.54	0.22	0.42
0.66	1.03	0.76	0.96	0.77	0.83	0.65	1.18	0.67	1.02	0.65	0.85
1.27	1.44	1.43	1.34	1.47	1.19	1.25	1.62	1.28	1.43	1.25	1.23
2.01	1.77	2.25	1.65	2.31	1.49	1.96	1.95	2.02	1.76	1.97	1.53
2.86	2.03	3.19	1.90	3.28	1.73	2.76	2.21	2.88	2.02	2.80	1.79
3.78	2.23	4.21	2.09	4.31	1.92	3.62	2.41	3.80	2.23	3.69	1.99
4.72	2.38	5.25	2.23	5.39	2.06	4.49	2.57	4.76	2.39	4.63	2.15
5.71	2.49	6.35	2.33	6.51	2.16	5.40	2.68	5.76	2.50	5.64	2.27
6.72	2.56	7.46	2.39	7.65	2.23	6.33	2.75	6.77	2.59	6.65	2.36
7.72	2.60	8.55	2.42	8.77	2.27	7.26	2.81	7.76	2.64	7.66	2.42
8.70	2.63	9.59	2.43	9.84	2.28	8.17	2.83	8.72	2.67	8.64	2.46
9.64	2.63	10.60	2.41	10.86	2.28	9.06	2.84	9.63	2.68	9.58	2.48
10.80	2.61	11.77	2.39	12.03	2.27	10.13	2.83	10.70	2.68	10.67	2.49
12.11	2.56	12.97	2.34	13.15	2.24	11.30	2.80	11.79	2.66	11.76	2.48
13.29	2.50	13.92	2.29	13.99	2.21	12.31	2.74	12.64	2.63	12.60	2.46
14.10	2.46	14.58	2.26	14.57	2.19	13.01	2.71	13.23	2.61	13.17	2.45
14.66	2.42	15.02	2.23	14.96	2.17	13.49	2.68	13.63	2.59	13.56	2.44

[a] The volume of excess adsorbed methane is reported in STP conditions; 1 mmol/g rock = 22.4 cm^3/g rock = 22.4 m^3/t rock = 791 scf/t rock.

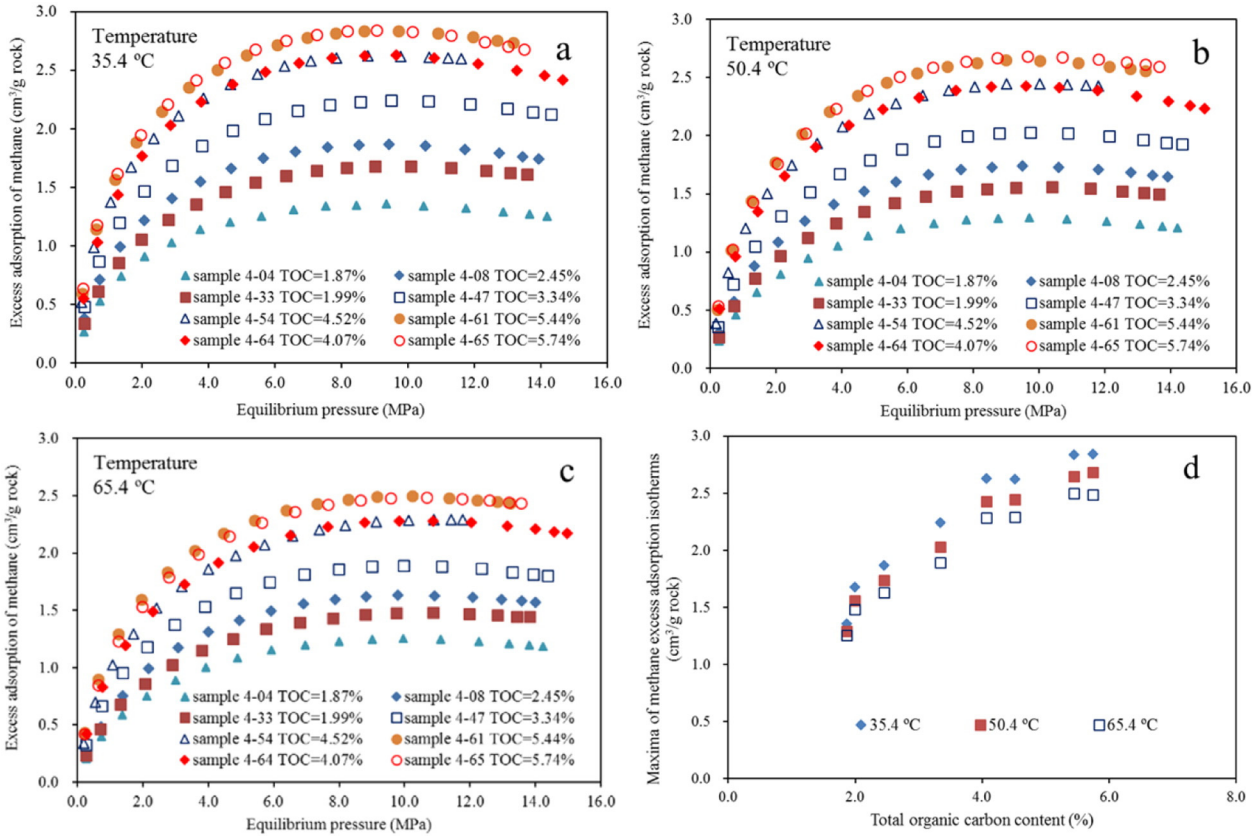

Fig. 4. Measured excess adsorption isotherms of methane at 35.4 °C (a), 50.4 °C (b), and 65.4 °C (c) for the eight samples.

pressure; and N is the total number of measured data points. During the fitting, the unknown parameters in Eqs. (5) and (6) were first fitted according to the rules that all of them, except for the D parameter, are expected to decrease with temperature (Hildenbrand et al., 2006; Gensterblum et al., 2013; Rexer et al., 2013). Once the fitted ρ_{ads} values are exceeding 424 mg/cm^3 (the density of liquid methane at its boiling temperature under 0.1 MPa), we adopted a constant ρ_{ads}, either 424 or 373 mg/cm^3 (based on the van der Waals volume, Gensterblum et al. (2013)), and a constant n_0 to refit the isotherms (e.g., Gasparik et al. (2012) and Gensterblum et al. (2013)).

2.5. Thermodynamic parameters of methane adsorption

The thermodynamic parameters of adsorption include enthalpy of adsorption (ΔH) and molar entropy of adsorption (ΔS^0), and are utilized to describe the pressure changes with temperature at a constant value of absolute adsorption (n) (Myers and Monson, 2002).

$$\ln\left(\frac{P}{P^0}\right)_n = \frac{\Delta H}{RT} - \frac{\Delta S^0}{R} \tag{8}$$

Table 3
Fitted temperature-dependent parameters of the SDR- and Langmuir-based excess adsorption models.

Sample			YC4-04	YC4-08	YC4-33	YC4-47	YC4-54	YC4-61	YC4-64	YC4-65
TOC (%)			1.87	2.45	1.99	3.34	4.52	5.44	4.07	5.74
SDR-based excess adsorption model	n_0 (cm^3/g rock)	35.4 °C	2.03	2.79	2.50	3.29	3.79	4.08	3.85	4.10
		50.4 °C	1.97	2.66	2.36	3.03	3.60	3.87	3.62	3.96
		65.4 °C	1.94	2.55	2.29	2.88	3.44	3.72	3.49	3.74
	ρ_{ads} (mg/cm^3)	35.4 °C	337.88	343.50	382.17	391.51	415.34	406.32	359.83	376.26
		50.4 °C	318.63	317.67	347.68	349.91	389.25	362.40	326.18	369.65
		65.4 °C	297.71	307.12	326.33	315.29	388.60	338.86	320.35	347.68
	D (mol^2·kJ^{-2})		0.0111	0.0112	0.0107	0.0101	0.0089	0.0088	0.0100	0.0092
	Δn (cm^3/g rock)		0.0017	0.0020	0.0020	0.0024	0.0016	0.0021	0.0028	0.0025
Langmuir-based excess adsorption model	n_0 (cm^3/g rock)	35.4 °C	1.86	2.59	2.26	2.94	3.13	3.45	3.51	3.51
		50.4 °C	1.86	2.59	2.23	2.73	3.00	3.28	3.40	3.42
		65.4 °C	1.86	2.59	2.17	2.72	2.88	3.19	3.27	3.25
	ρ_{ads} (mg/cm^3)	35.4 °C	454.87	486.55	609.91	635.05	1027.00	894.91	513.42	728.89
		50.4 °C	408.82	400.77	476.54	571.98	940.69	787.76	430.70	702.30
		65.4 °C	386.42	362.27	461.05	429.27	940.69	705.95	438.19	674.51
	K_L (MPa^{-1})	35.4 °C	1.24	0.48	0.49	0.54	1.90	0.74	0.57	0.73
		50.4 °C	1.06	0.38	0.40	0.48	1.66	0.66	0.48	0.58
		65.4 °C	0.96	0.30	0.35	0.40	1.39	0.56	0.40	0.49
	Δn (cm^3/g rock)		0.0117	0.0040	0.0039	0.0055	0.0164	0.0072	0.0068	0.0074

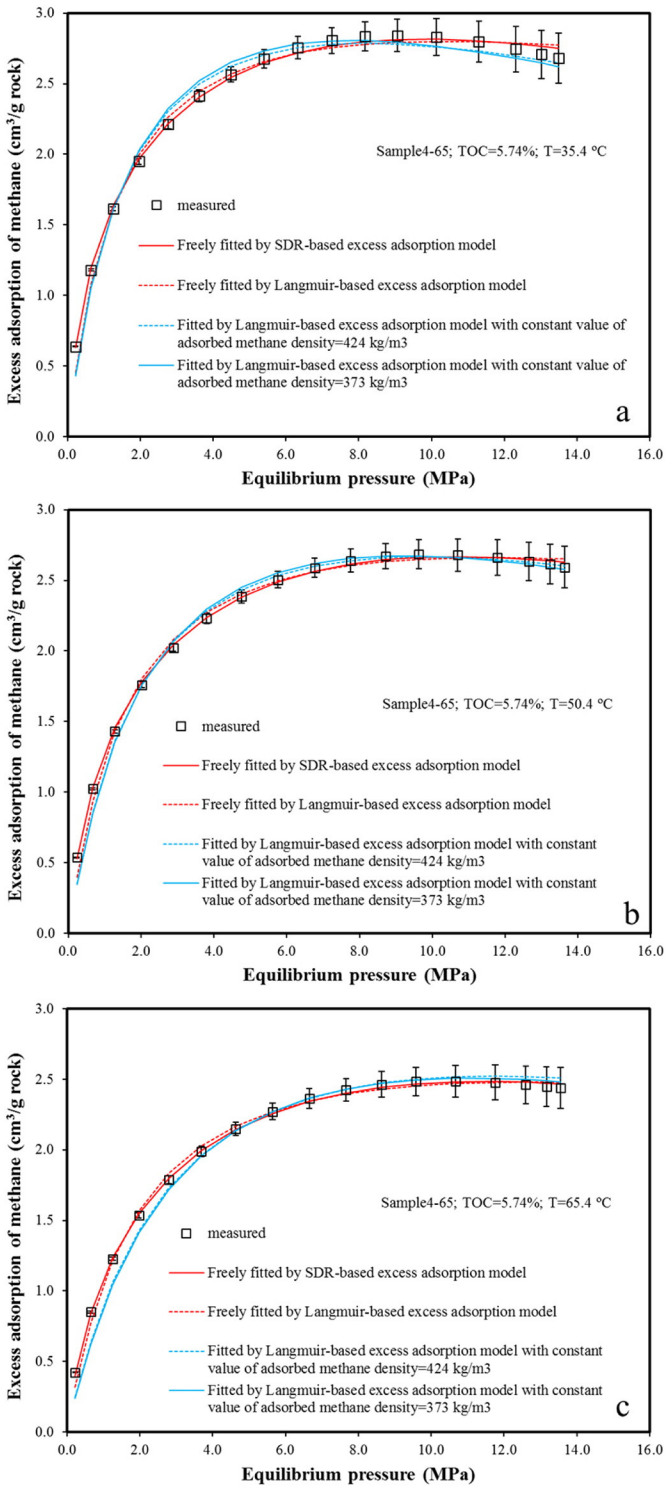

Fig. 5. An example showing the fitting quality using various methods. The experimental uncertainty increases with pressure and is about 0.15–0.18 cm^3/g rock at 14 MPa under different temperatures, close to those reported by Gasparik et al. (2012).

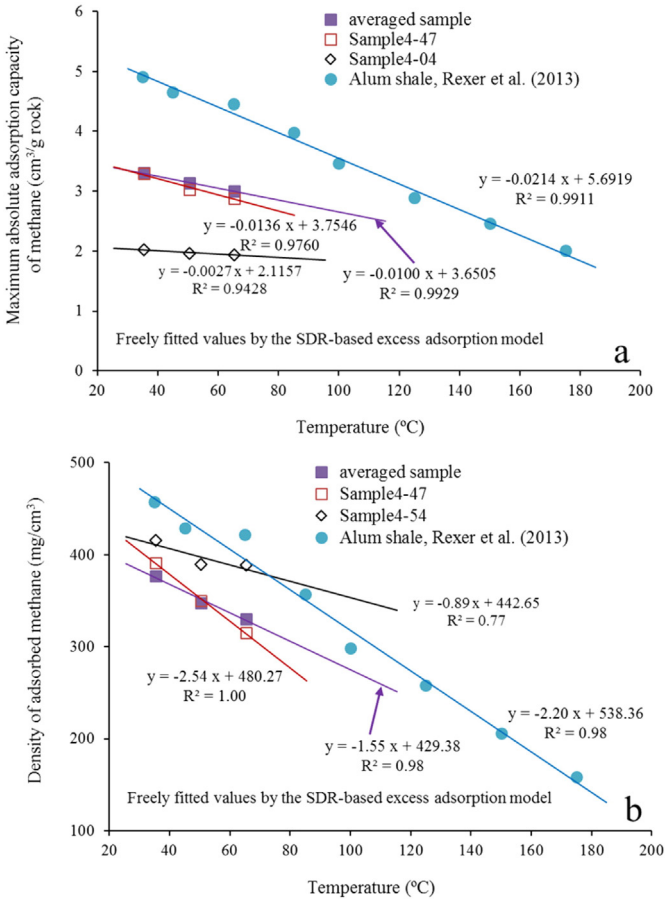

Fig. 6. An example showing the temperature dependence of maximum absolute adsorption capacity of methane (a) and density of adsorbed methane (b) fitted by the SDR-based excess adsorption model. The data from Rexer et al. (2013) is used to illustrate that the temperature dependence could be valid at high temperatures.

Where p^0 is the atmospheric pressure (0.1 MPa) and the isosteric heat of adsorption (Q_{st}) is equal to the enthalpy of adsorption but with a negative sign ($Q_{st} = -\Delta H$). Then the Q_{st} and ΔS^0 can be derived from the slope and the y-axis intercept, respectively, of the plot of ln(P) versus 1/T.

3. Results

3.1. TOC, organic petrology, and mineralogical composition

The total organic carbon (TOC) contents for the eight shale samples range between 1.87 and 5.74% (Table 1). The organic fraction is dominated by maceral assemblages of micrinite, interpreted as the residual amorphous organic matter after oil generation and expulsion (Stach et al., 1982; Ross and Bustin, 2009), and pyrobitumen formed by the cracking of retained oil in shales (Fig. 2; Pepper and Dodd, 1995; Bernard et al., 2012; Mahlstedt and Horsfield, 2012). The random pyrobitumen reflectance was found to be in the range of 2.64–3.62% (Table 1). The calculated equivalent vitrinite reflectances using the equation of Schoenherr et al. (2007) are in the range of 2.75–3.68%Ro, reaching the overmature stage. The mineralogical compositions of the eight black shale samples are also listed in Table 1. Their clay contents are in the range of 28.1–59.7% and are dominated by illite and chlorite. The quartz and feldspar contents range from 25.4 to 59.0% and from 5.2 to 16.6%, respectively, whereas the carbonate contents vary from below the detection limit to 9.9%.

3.2. Low-pressure N_2 adsorption

Using the N_2 adsorption isotherms at 77.4 K, total specific surface areas (S_{BET}) were determined by the BET equation. The values range from 12.5 to 20.6 m^2/g (Table 1). The micropore surface areas (S_{DR}) and volumes (V_{DR}) by the DR equation are in the range of 6.6–10.8 m^2/g and 4.7–7.6 cm^3/kg, respectively. The surface areas of

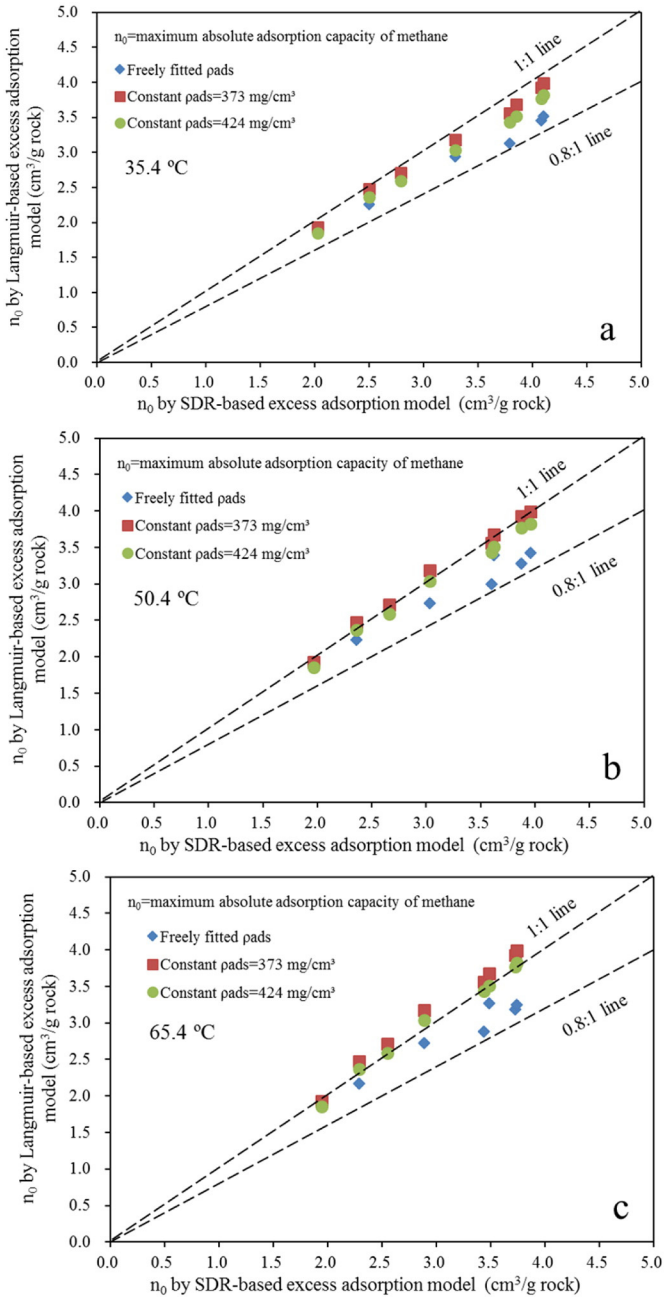

Fig. 7. Relationship of the maximum absolute adsorption capacities of methane fitted by the SDR-based excess adsorption model to those fitted by the Langmuir-based excess adsorption model with a constant or variable density of adsorbed methane.

meso-/macropores (>2 nm in diameter,S_{BJH}) were estimated by the BJH model and range between 5.8 to 12.3 m^2/g. A positive correlation is observed between the TOC and surface area/micropore volume (Fig. 3a), but the total clay content is largely inversely correlated with the latter (Fig. 3b), indicating that the organic matter is the main contributor to both the surface areas and micropores of shales (Ross and Bustin, 2009).

3.3. Excess adsorption of methane

The measured excess adsorbed amounts of methane at different temperatures are presented in the unit of cm^3/g rock under STP conditions and listed in Table 2. As illustrated in Fig. 4, the excess adsorbed amount of methane (n_{excess}) increases at first with increasing pressures at all experimental temperatures and reaches a maximum value at a certain pressure (around 10 MPa), after which the n_{excess} begins to slightly decrease with pressures. This phenomenon, also encountered in previous studies (Gasparik et al., 2012, 2014a; Rexer et al., 2013; Tan et al., 2014a), is caused by the fact that the n_{excess} is calculated on the basis of the void volume measured before the adsorption experiment by implicitly assuming that the void volume remains unchanged during experiment (i.e., the volume occupied by the adsorbed gas was assumed negligible). This assumption is acceptable as long as the density of the free gas phase is much lower than the density of the adsorbed gas. As expected from Eqs. (1) and (2), the n_{excess} will approach zero when the pressure is high enough and the density of methane in free state approaches the density of adsorbed methane; this inference has been verified by experiments with CO_2 adsorption on activated carbon and shales under very high pressures (Gensterblum et al., 2009; Chareonsuppanimit et al., 2012; Gasparik et al., 2014b).

As revealed by Fig. 4d, the maxima of the excess methane adsorption isotherms ($n_{\max}^{excess}$) are positively related to the TOC content at all experimental temperatures. Furthermore, samples have very similar excess adsorption characteristics throughout experimental pressure range when their TOCs are similar, which can be clearly seen for samples 4–61 and 4–65, and for samples 4–54 and 4–64 (Fig. 4a, b, and c). These observations are consistent with previous results and further illustrate that TOC is an important control on the methane adsorption on shales because organic matter provides a large specific surface area (Chalmers and Bustin, 2007, 2008; Ross and Bustin, 2009; Zhang et al., 2012; Gasparik et al., 2014a).

3.4. Fitted parameters of the SDR-based excess adsorption model

The fitted parameters of the SDR-based excess adsorption model (Eq. (6)) are listed in Table 3, and an example for the comparison of fitted and measured results is presented in Fig. 5. The fitted values of n_0 range from 2.03 to 4.10 cm^3/g rock at 35.4 °C, 1.97 to 3.96 cm^3/g rock at 50.4 °C and 1.94 to 3.74 cm^3/g rock at 65.4 °C; the fitted values of ρ_{adsT} range from 338 to 415 mg/cm^3 at 35.4 °C, 319 to 389 mg/cm^3 at 50.4 °C and 298 to 389 mg/cm^3 at 65.4 °C. The fitted adsorbed gas

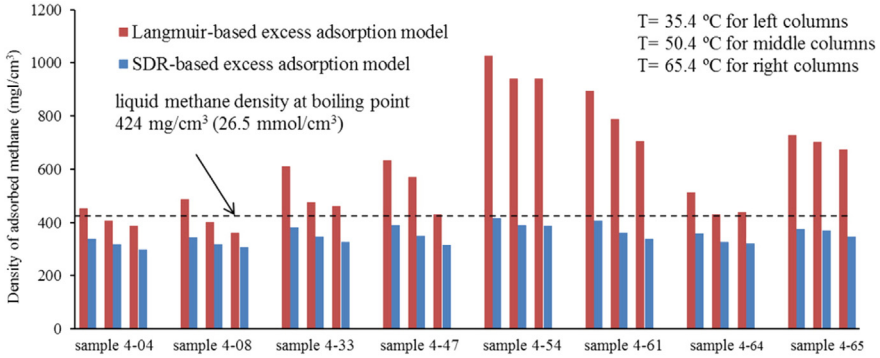

Fig. 8. Comparison of the temperature-dependent densities of adsorbed methane fitted by the SDR- and Langmuir-based excess adsorption models.

Table 4
Fitted parameters of the Langmuir-based excess adsorption model with constant density and maximum capacity of adsorbed methane.

Sample		YC4-04	YC4-08	YC4-33	YC4-47	YC4-54	YC4-61	YC4-64	YC4-65
TOC (%)		1.87	2.45	1.99	3.34	4.52	5.44	4.07	5.74
Temperature-independent n_0 (cm^3/g rock)		1.93	2.71	2.48	3.18	3.56	3.93	3.68	3.99
Temperature-independent ρ_{ads} (mg/cm^3)		373	373	373	373	373	373	373	373
	35.4 °C	1.19	0.46	0.43	0.50	1.53	0.60	0.55	0.58
Temperature-dependent K_L (MPa^{-1})	50.4 °C	0.98	0.34	0.32	0.35	1.16	0.44	0.39	0.43
	65.4 °C	0.87	0.26	0.26	0.27	0.90	0.34	0.30	0.31
Δn (cm^3/g rock)		0.0126	0.0055	0.0058	0.0102	0.0219	0.0126	0.0101	0.0112
Temperature-independent n_0 (cm^3/g rock)		1.85	2.59	2.37	3.04	3.44	3.77	3.51	3.82
Temperature-independent ρ_{ads} (mg/cm^3)		424	424	424	424	424	424	424	424
	35.4 °C	1.30	0.51	0.47	0.55	1.65	0.65	0.61	0.63
Temperature-dependent K_L (MPa^{-1})	50.4 °C	1.06	0.37	0.35	0.38	1.25	0.48	0.43	0.46
	65.4 °C	0.94	0.29	0.28	0.29	0.95	0.37	0.33	0.34
Δn (cm^3/g rock)		0.0124	0.0054	0.0055	0.0098	0.0211	0.0116	0.0097	0.0103

density values are lower than that of liquid methane at its boiling point (424 mg/cm^3 at −161 °C and 0.1 MPa).

The fitted values of ρ_{ads} and n_0 are both temperature dependent (Fig. 6). The averaged reduction rate of fitted n_0 for the eight samples is about 0.01 cm^3/g/°C, with the maxima of 0.0136 cm^3/g/°C for sample 4–47 and minima of 0.0027 cm^3/g/°C for sample 4–04 (Fig. 6a). The temperature-dependence of maximum absolute adsorption capacity of methane on coals was also reported by Hildenbrand et al. (2006). More recently, Rexer et al. (2013) studied the maximum absolute adsorption capacity of methane using the SDR-based excess adsorption model at temperatures up to 175 °C and found that the reduction rate of n_0 is about 0.0214 cm^3/g/°C for an Alum shale sample from Denmark (Fig. 6a). The reduction rate of ρ_{ads} ranges from the smallest value of 0.89 mg/cm^3/°C for sample 4–54 to the largest value of 2.54 mg/cm^3/°C for sample 4–47, with an average value of 1.55 mg/cm^3/°C (Fig. 6b). This is quite close to the value of 2.2 mg/cm^3/°C reported by Rexer et al. (2013) for an Alum shale sample at an experimental temperature range of 35–175 °C.

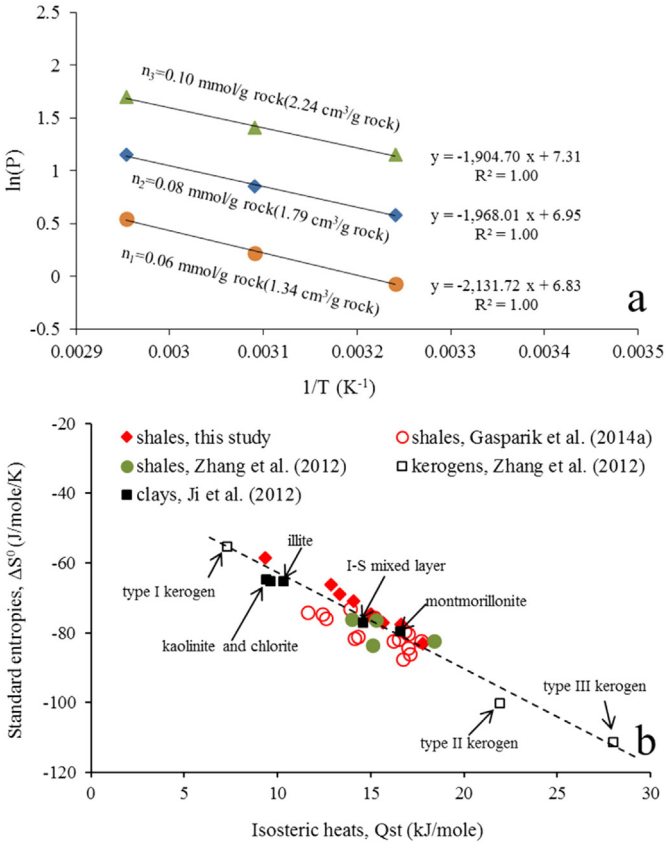

Fig. 9. Plot of natural logarithm pressure versus reciprocal of temperature showing the determination of isosteric heat and standard entropy at three different absolute adsorption amounts (a; sample 4–54), and the linear relationship between the averaged isosteric heats and standard entropies for our eight samples and other shales and clays (b).

The third parameter in the SDR-based excess adsorption model is the D value (in $mol^2 \cdot kJ^{-2}$), which ranges from 0.0088 to 0.0112. Rexer et al. (2013) reported a D value of 0.0092 for one Alum shale sample obtained from the Skelbro-2 well in Bornholm, Denmark. Clarkson and Haghshenas (2013) also calculated the D values for some shales using published methane adsorption dataset. For example, the D value is 0.02 for the Rio Bonito carbonaceous shales in Brazil (Weniger et al., 2010), 0.013 for the New Albany shales in USA (Chareonsuppanimit et al., 2012), and is in the range of 0.0134–0.0135 for the Montney, Duvernay and Muskwa shales in Canada (Beaton et al., 2010). The slight difference in D values between various shales is mainly related to the difference in their pore structures and surface chemistry (White et al., 2005).

3.5. Fitted parameters of the Langmuir-based excess adsorption model

3.5.1. Fitting with temperature-dependent ρ_{ads} and n_0

Despite relatively large deviations for some data points at low pressures, the Langmuir-based excess adsorption model (Eq. (5)) fits the measured isotherms nearly as good as the SDR-based excess adsorption model does (Table 3, Fig. 5). Although the n_0 values are slightly smaller for samples with TOC values of larger than 2.7%, they are linearly correlated to those by the SDR-based excess adsorption model (Fig. 7). Note that the values of ρ_{ads} fitted by the Langmuir-based excess adsorption model are much larger than those fitted by the SDR-based excess adsorption model and also by far exceed the value of 424 mg/cm^3 (Fig. 8). The very large ρ_{ads} values were also reported by other authors. For example, Gasparik et al. (2014a) reported that the ρ_{ads} values freely fitted by the Langmuir-based excess adsorption model at 65 °C ranges from 500 to 637 mg/cm^3 for some Barnett shales and as high as 790 mg/cm^3 for one Haynesville shale sample. Hu et al. (2015) even applied an adsorbed density of 800 mg/cm^3 to fit the excess adsorption of methane on artificially matured Woodford shales. The third parameter K_L (in MPa^{-1}) ranges from 0.48 to 1.90 at 35.4 °C, 0.38 to 1.66 at 50.4 °C, and 0.30 to 1.39 at 65.4 °C, falling in the ranges reported by other authors for shales and kerogens (Zhang et al., 2012; Gasparik et al., 2014a; Hu et al., 2015).

3.5.2. Fitting with a fixed density value of adsorbed methane

Considering that the freely fitted ρ_{ads} values by the Langmuir-based excess adsorption model are very large and exceed the liquid density of methane at its boiling point (424 mg/cm^3), we conducted the fitting again by setting a temperature-independent and constant value of ρ_{ads}

Table 5
Isosteric heats (Q_{st}) and standard adsorption entropies (ΔS^0) obtained at different absolute methane adsorption amounts (n).

Sample	n_0 at 35.4 °C	n_1	Q_{st}	ΔS^0	n_2	Q_{st}	ΔS^0	n_3	Q_{st}	ΔS^0	Average Q_{st}	Average ΔS^0
	cm^3/g rock	cm^3/g rock	kJ/mol	J/mol/K	cm^3/g rock	kJ/mol	J/mol/K	cm^3/g rock	kJ/mol	J/mol/K	kJ/mol	J/mol/K
YC4-04	2.0	0.9	10.6	−58.6	1.1	9.0	−57.5	1.3	8.5	−59.6	9.4	−58.6
YC4-08	2.8	1.1	14.3	−68.9	1.3	13.2	−68.6	1.6	12.5	−69.2	13.3	−68.9
YC4-33	2.5	0.9	15.2	−72.1	1.1	14.6	−73.4	1.3	15.1	−78.2	15.0	−74.6
YC4-47	3.3	1.3	14.8	−70.5	1.6	14.0	−70.7	1.8	13.4	−71.4	14.1	−70.9
YC4-54	3.8	1.3	17.3	−74.7	1.8	16.1	−76.1	2.2	15.6	−79.3	16.4	−76.7
YC4-61	4.1	1.6	13.9	−64.7	2.0	12.7	−65.8	2.5	12.0	−66.3	12.9	−65.6
YC4-64	3.9	1.3	19.1	−82.3	1.8	17.5	−82.5	2.2	16.8	−84.4	17.8	−83.1
YC4-65	4.1	1.8	17.5	−78.4	2.2	15.4	−76.4	2.7	15.3	−80.2	16.1	−78.3

to be 424 or 373 mg/cm^3, and then assuming that both the ρ_{ads} and n_0 values are constant at different temperatures (e.g., Gensterblum et al. (2014b) and Bruns et al. (2016)). Compared with the fitting quality when taking absorbed methane density as a variable, a relatively poor fitting was observed in the low pressure range, but a fairly good fitting in the high pressure range (Table 4; Fig. 5). Gensterblum et al. (2013) illustrated that a low value of ρ_{ads} led to a high value of n_0, which is also observed in our study (Table 4, Fig. 7). Nevertheless, no significant difference in the maximum absolute methane adsorption capacity between the SDR- and Langmuir-based excess adsorption models was observed when the density of adsorbed methane is presumed to be 373 or 424 mg/cm^3 (Fig. 7). Our comparative studies provided further evidence that a constant ρ_{ads} used by some authors is a valid approach (e.g., Gasparik et al. (2012); Gensterblum et al. (2014b) and Bruns et al. (2016)).

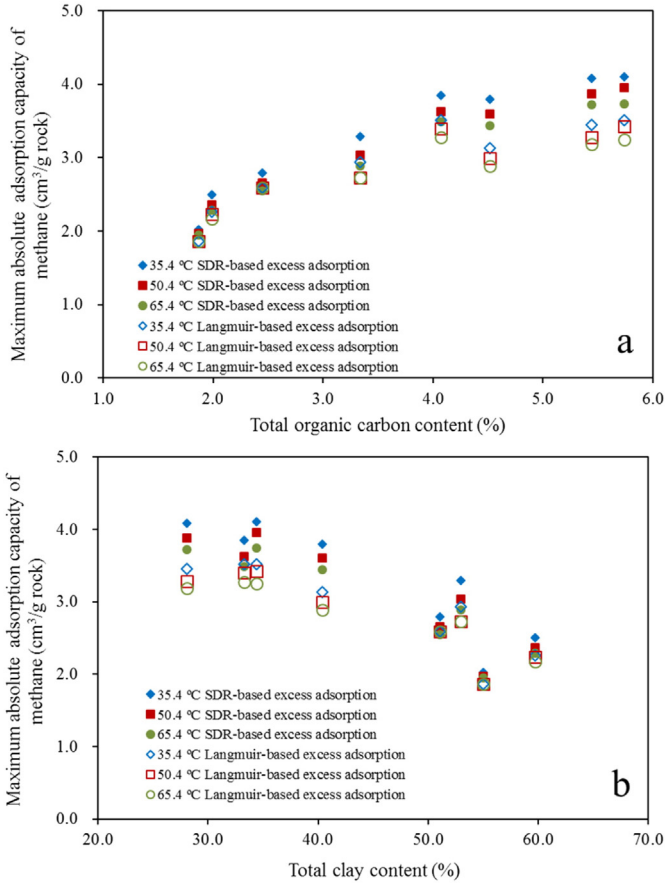

Fig. 10. Relationship of TOC (a) and total clay content (b) with the maximum absolute adsorption capacity of methane freely fitted by the SDR- and Langmuir-based excess adsorption models in which the density of adsorbed methane is presumed to be temperature dependent.

3.6. Thermodynamic parameters of adsorption

Based on the absolute adsorption amount of methane calculated by the SDR-based excess adsorption model, the thermodynamic parameters of methane adsorption can be determined by the plot of 1/T versus ln(P). As illustrated in Fig. 9a, the isosteric heat and entropy of adsorption decrease slightly with increased absolute adsorption amounts of methane, which was also observed by Rexer et al. (2013). Therefore, the isosteric heats and adsorption entropies were calculated for three different absolute amounts of adsorbed gas (fractional occupancy; n_1, n_2 and n_3) and listed in Table 5. Among them, the second absolute adsorbed amount (n_2) is approximately half of the maximum absolute adsorption capacity (n_0) at 35.4 °C, while the first (n_1) and third (n_3) amounts are somewhat lower and higher than n_2, respectively. In other studies, the thermodynamic parameters were only calculated at the Langmuir pressure, corresponding to half of the maximum adsorption capacity (Ji et al., 2012; Zhang et al., 2012; Gasparik et al., 2014a).

The averaged isosteric heats (Q_{st}) vary from 9.4 to 17.8 kJ/mol and the averaged adsorption entropies (ΔS^0) vary between −58.6 and −83.1 J/mol/K (Table 4); both are close to the values calculated at the second absolute adsorption amount (n_2), which is nearly half of the maximum absolute adsorption capacity (n_0) at 35.4 °C. A linear relationship exists between the isosteric heat and adsorption entropy (Fig. 9b); all the data fall between the end members of the type I/II kerogen and the main minerals in shales (Ji et al., 2012; Zhang et al., 2012) and are consistent with the results of Gasparik et al. (2014a).

4. Discussion

4.1. Effects of organic and inorganic matters on n_0

As illustrated in Fig. 10a, a largely positive correlation is observed between TOC content and maximum absolute adsorption capacity of methane (n_0). This relationship was also reported for many other shales (Weniger et al., 2010; Zhang et al., 2012; Gasparik et al., 2014a) and is mainly attributed to the fact that TOC is positively correlated with total surface area and micropore volume (Fig. 3a). The relationship of n_0 with total clay, however, is quite complex (Fig. 10b). For samples with high content of total clay (>35%), the n_0 decreases with increasing total clay, whereas it changes little for two samples whose total clay content is less than 35%. This negative correlation is probably related to the different methane adsorption capacities of clays and organic matters. The composition of clay minerals for our samples is dominated by illite and chlorite (Table 1). As illustrated by Ji et al. (2012), the specific methane adsorption capacity of illite and chlorite is only 1.8 cm^3/g and 2.3 cm^3/g, whereas the methane adsorption capacity of type I/II kerogen is as high as 27.3–32.7 cm^3/g TOC (Zhang et al., 2012). Gasparik et al. (2012) reported a significant contribution of clays to methane adsorption on organic-lean shales of low thermal maturity; their samples have relatively lower thermal maturity and the composition of clay minerals is dominated by an illite–smectite mixed layer that has a methane adsorption capacity two times larger than that of illite and chlorite (Ji et al., 2012; Gasparik et al., 2014a).

Table 6
Averaged adsorption parameters adopted in Figs. 11 and 12 for the eight samples.

Model name	Adsorption model	n_o (cm^3/g rock)	ρ_{ads} (mg/cm^3)	K_L (MPa^{-1})	D ($mol^2 \cdot kJ^{-2}$)
Model 1	SDR-based excess adsorption	$-0.010 \times T + 3.650$	$-1.545 \times T + 429.39$	n.a.	0.00989
Model 2	Langmuir-based excess adsorption	$-0.005 \times T + 3.097$	$-3.97 \times T + 802.83$	$-0.008 \times T + 1.103$	n.a.
Model 3	Langmuir-based excess adsorption	3.05	424	$-0.0109 \times T + 1.169$	n.a.
Model 4	Langmuir-based excess adsorption	3.18	373	$-0.0097 \times T + 1.066$	n.a.

n.a.: not applicable and T is the temperature in °C.

4.2. Comparison of different models on geological gas-in-place (GIP) estimation

Based on the adsorption parameters obtained by various methods, the absolute and excess methane sorption capacity of shales and coals can be tentatively extrapolated to geological conditions as previous authors did (e.g., Hildenbrand et al. (2006); Gensterblum et al. (2014b) and Bruns et al. (2016)). However it should be noticed that the moisture in shales could significantly reduce their methane sorption capacity and that there are probably no shales completely devoid of moisture at geological conditions (Chalmers and Bustin, 2008; Busch and Gensterblum, 2011; Gasparik et al., 2014a; Gensterblum et al., 2014a). Therefore the geological extrapolation based on the dry adsorption data should be regarded as a maximum scenario (Bruns et al., 2016).

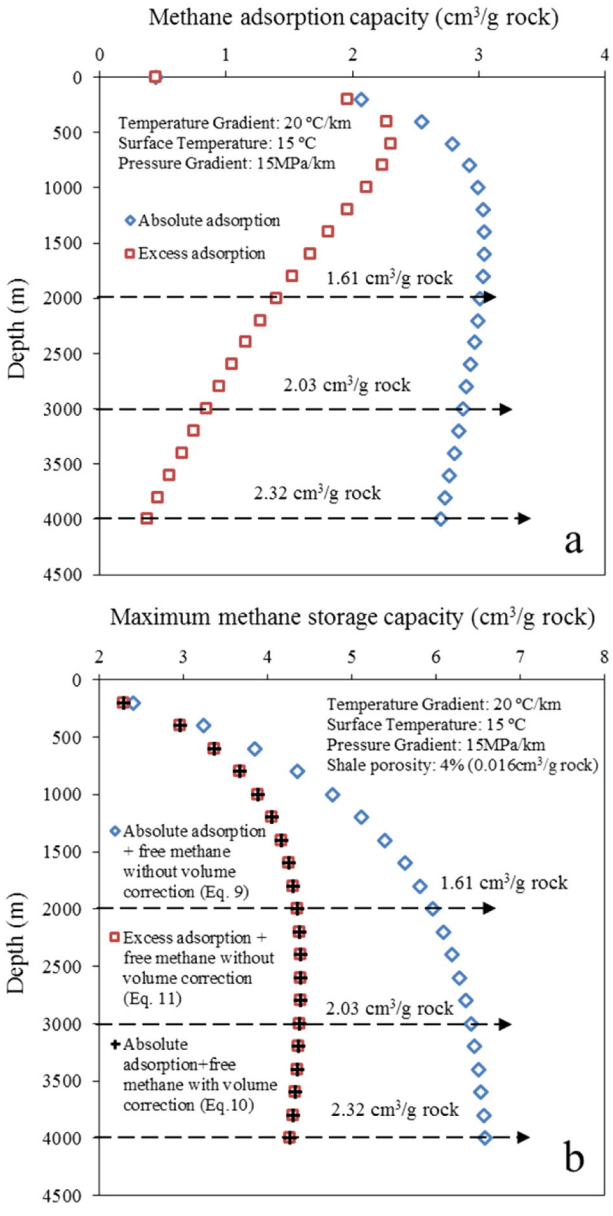

Fig. 11. Plots showing the absolute and excess methane adsorption profiles with depth (a) and the calculated GIP depth-profiles by Eqs. (9)–(11) (b) on the basis of methane adsorption parameters fitted by the SDR-based excess adsorption model as listed in Table 6. The density of free methane was calculated according to the high-accuracy equation of state (EoS) of Setzmann et al. (1991).

4.2.1. Excess versus absolute adsorption models

Gas-in-place (GIP) must estimate the sum of adsorbed and free gas. Frequently, adsorbed gas (n_{sorb}) is calculated using absolute adsorption models such as the two-parameter Langmuir model; the calculation of free gas capacity (n_{free}) is based on the measured porosity and the free gas density under given temperatures and pressures (Eq. (9); Luffel and Guidry, 1992; Mavor and Nelson, 1997).

$$GIP = n_{free} + n_{sorb} = n_{free} + n_{abs} \tag{9}$$

Ambrose et al. (2012) pointed out that measured porosity values used in the calculation of free gas capacity must be corrected by subtracting the volume occupied by adsorbed gas (Eq. (10)) when an absolute adsorption model is chosen to calculate the capacity of adsorbed gas. Otherwise, the GIP would be overestimated because the volume of adsorbed gas is accounted for in duplicate for both free gas and adsorbed gas capacities.

$$GIP = n_{free} - \rho_g \cdot V_{ads} \cdot C_{STP} + n_{abs} \tag{((10)))}$$

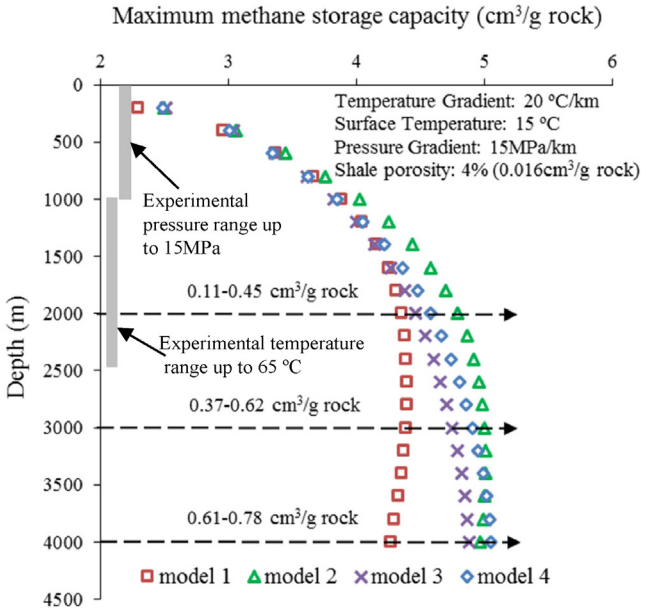

Fig. 12. A comparison of gas-in-place (GIP) profiles with depth calculated by Eq. (11) on the basis of various models listed in Table 6.

Substituting Eq. (2) into Eq. (10) yields Eq. (11),

$$GIP = n_{free} + n_{excess} \quad (11)$$

Thus, the measured porosity can be used directly to calculate the free gas capacity without any volume correction when it is combined with the experimentally measured excess sorption capacity. The expression of the GIP in Eq. ((11) is consistent with the experimental data that are inherently excess sorption capacities and can be presented by either Langmuir- or SDR-based excess sorption models, and no volumetric corrections are needed when applied to basin modeling (e.g., Bruns et al. (2016)).

On the basis of the adsorption parameters fitted by the SDR-based excess model as listed in Table 6, the differences between the absolute and excess adsorption amount and the corresponding estimated GIPs with Eqs. (9), (10) and (11) are presented in Fig. 11. Our case model is constructed for an overpressured system with a pressure coefficient of 1.5 and a geothermal gradient of 20 °C/km, assuming a shale porosity of 4% (pore volume value of 0.016 cm^3/g rock) with 100% gas saturation. These geological parameters are largely representative of the producing shale-gas reservoirs in the study area (Guo and Zhang, 2014; Wei and Wei, 2014). It is evident that the absolute adsorption profile begins to deviate from the excess adsorption profile at very shallow depths and the former is about 1.61–2.32 cm^3/g rock larger than the latter at depths of 2000–4000 m (Fig. 11a). Accordingly, the GIPs by the Eq. ((9) without volumetric correction in the free gas capacity are also approximately 1.61–2.32 cm^3/g rock larger than those after pore volume correction by the Eq. ((10) or ((11) at depths of 2000–4000 m (Fig. 11b). The other merit of the present method is that it mathematically provides a simple way to evaluate the maximum GIP in history for shales that were ever subject to very high temperature and pressure because at the time when their excess methane adsorption capacity approached zero, their GIPs could be represented simply by the free gas storage capacity without any volumetric correction. With the shales being uplifted, the gas stored in them would be inevitably lost due to various causes, thus leading to a decrease in GIP though geological time unless new gas has been supplied.

4.2.2. SDR- versus Langmuir-based excess adsorption models

As listed in Table 6, both the density and the maximum capacity of adsorbed methane vary among different models, which probably leads to a variation in the GIP estimation when extrapolated to the geological conditions beyond the experimental temperature and pressure. On the basis of the various adsorption model parameters listed in Table 6, the depth-profiles of GIP calculated by the Eq. (11) are compared in Fig. 12 under the same geological conditions as in Fig. 11. It is evident that all the models predict virtually the same GIPs at depths of less than 1000 m, but some deviation occurs at depths greater than 1000 m (beyond the maximum experimental pressure 15 MPa), with the SDR-based excess model predicting a smaller GIP than the Langmuir-based excess models. The difference is about 0.11–0.45 cm^3/g rock at a depth of 2000 m and 0.61–0.78 cm^3/g rock at a depth of 4000 m, respectively (Fig. 12), much smaller than those caused by the double counting of the volume of adsorbed methane (Fig. 11b).

At present, it is hard to evaluate which model is more accurate because the uncertainty of experimental data becomes greater at high pressures (Gasparik et al., 2012, 2014b) and all models can fit experimental data fairly good within the experimental errors at high pressures (Gasparik et al., 2012, 2014a; Gensterblum et al., 2013). Therefore, much work has to be carried out in the future on the reduction of experimental errors at high pressure ranges (Gasparik et al., 2014a). Nevertheless our results show that it is convenient and feasible to adopt a constant value of adsorbed methane density, either 424 mg/cm^3 or 373 mg/cm^3, and a constant value of maximum absolute adsorption capacity, when the Langmuir-based excess adsorption model is selected to fit the measured excess isotherms (Gensterblum et al., 2013, 2014b; Bruns et al., 2016). When it comes to the temperature-dependent values of adsorbed methane density and its absolute adsorption capacity, the SDR-based excess model seems to be more reliable because it predicts a more reasonable density of adsorbed methane that never exceeds the liquid density of methane at its boiling point (i.e., 424 mg/cm^3) at our experimental temperatures.

5. Conclusions

(1) Total organic carbon (TOC) is a key parameter that dominates methane adsorption capacity because organic matter is the main contributor to specific surface area and micropore volume for shale samples.

(2) Both the SDR- and Langmuir-based excess adsorption models can be used to fit the experimental excess adsorption isotherms within the experimental temperature and pressure range of this study with good precision. The temperature-dependent densities of adsorbed methane resulting from the fitting procedure with the SDR-based excess adsorption model are generally smaller than the density of liquid methane at its boiling point, i.e., 424 mg/cm^3, whereas the nominal adsorbed phase densities resulting from the Langmuir-based excess adsorption model are much larger than 424 mg/cm^3. Nevertheless, the maximum methane adsorption capacities fitted by both models are not significantly different and are, in fact, linearly correlated with each other.

(3) While early studies have illustrated that avoiding the double counting of the volume of adsorbed gas is the first step in getting a consistent GIP estimate, our results further show that the adsorption model itself, either the Langmuir- or SDR-based excess adsorption model, and the fitting procedure, either constant or temperature-dependent density and maximum capacity of adsorbed methane, do not significantly affect the estimated GIPs for the geological system in our study area at depths of less than 4000 m.

Acknowledgments

The authors are grateful to Prof. Ralf Littke and two anonymous reviewers for their insightful comments and suggestions that have significantly improved the manuscript. This study was jointly supported by the Strategic Priority Program of the Chinese Academy of Sciences (Grant No. XDB10040300), the National Natural Science Foundation of China (Grant No. 41522302) and the National Key Basic Research Program of China (973 Program: 2012CB214705). Hui Tian is also grateful to the Youth Innovation Promotion Association, CAS, for financial support. This is contribution No. IS-2186 from GIGCAS.

Appendix 1. Parameters and units used in equations

C_{STP}	Coefficient of a unit conversion from mass to volume, cm^3/mg under STP conditions;
D	Pore-structure parameter, $mol^2 \cdot kJ^{-2}$;
GIP	Gas-in-place, cm^3/g rock under STP conditions;
ΔH	Enthalpy of adsorption, kJ/mol;
K_L	Langmuir constant, MPa^{-1};
N	Total number of measured data points (dimensionless);
Δn	Fitting error, cm^3/g rock under STP conditions;
$n_i^{exp}(p_i,T_i)$	Measured excess adsorption amount at the ith paired temperature and pressure, cm^3/g rock under STP conditions;
$n_i^{fit}(p_i,T_i)$	Fitted excess adsorption amount at the ith paired temperature and pressure, cm^3/g rock under STP conditions;
n_0	Maximum absolute methane adsorption capacity, cm^3/g rock under STP conditions;
n_{abs}	Absolute methane adsorption capacity, cm^3/g rock under STP conditions;

n_{excess} Excess methane adsorption capacity, cm^3/g rock under STP conditions;
n_{free} Free gas storage capacity, cm^3/g rock under STP conditions;
n_{sorb} Adsorbed gas storage capacity, cm^3/g rock under STP conditions;
P Pressure, MPa;
P^0 Atmospheric pressure (0.1 MPa);
P_L Langmuir pressure, MPa;
Q_{st} Isosteric heat of adsorption, kJ/mol;
R Ideal gas constant (8.314×10^{-3} kJ·mol^{-1}·K^{-1});
ΔS^0 Molar entropy of adsorption, J/mol/K;
T Temperature in Kelvin (K);
V_{ads} Volume of adsorbed gas phase, cm^3/g rock;
ρ_{ads} Density of adsorbed gas phase, mg/cm^3;
ρ_g Density of free gas phase, mg/cm^3

Appendix 2. Unit conversion

For methane amount in volume and mass: 1 mmol/g rock = 16 mg/g rock = 22.4 cm^3 (STP)/g rock = 22.4 m^3 (STP)/t rock = 791 scf (STP)/t rock.

For temperature in Celsius and Kelvin: 1 °C = 273.15 K.

References

Ambrose, R.J., Hartman, R.C., Diaz-Campos, M., Akkutlu, I.Y., Sondergeld, C.H., 2012. Shale gas-in-place calculations. Part I: new pore-scale considerations. SPE J. 17, 219–229.

Beaton, A.P., Pawlowicz, J.G., Anderson, S.D.A., Berhane, H., Rokosh, C.D., 2010. RockEvalTM, total organic carbon and adsorption isotherms of the Duvernay and Muskwa formations in Alberta: shale gas data release. Energy Resources Conservation Board/Alberta. Geological Survey Open File Report (2010-04).

Bernard, S., Wirth, R., Schreiber, A., Schulz, H.M., Horsfield, B., 2012. Formation of nanoporous pyrobitumen residues during maturation of the Barnett Shale (Fort Worth Basin). Int. J. Coal Geol. 103, 3–11.

Bruns, B., Littke, R., Gasparik, M., van Wees, J.-D., Nelskamp, S., 2016. Thermal evolution and shale gas potential estimation of the Wealden and Posidonia Shale in NW-Germany and the Netherlands: a 3D basinmodelling study. Basin Res. 28, 2–33.

Busch, A., Gensterblum, Y., 2011. CBM and CO_2-ECBM related sorption processes in coal: a review. Int. J. Coal Geol. 87, 49–71.

Chalmers, G.R.L., Bustin, R.M., 2007. The organic matter distribution and methane capacity of the Lower Cretaceous strata of northeastern British Columbia, Canada. Int. J. Coal Geol. 70, 223–339.

Chalmers, G.R.L., Bustin, R.M., 2008. Lower Cretaceous gas shales in northeastern British Columbia. Part I: geological controls on methane sorption capacity. Bull. Can. Petrol. Geol. 56, 1–21.

Chareonsuppanimit, P., Mohammad, S.A., Robinson Jr., R.L., Gasem, K.A.M., 2012. High-pressure adsorption of gases on shales: measurements and modeling. Int. J. Coal Geol. 95, 34–46.

Chen, S., Zhu, Y., Wang, H., Liu, H., Wei, W., Fang, J., 2011. Shale gas reservoir characterization: a typical case in the southern Sichuan Basin of China. Energy 36, 6609–6616.

Clarkson, C.R., Haghshenas, B., 2013. Modeling of supercritical fluid adsorption on organic-rich shales and coal. Soc. Pet.Eng. (Paper No. SPE 164532, 24 p).

Curtis, J.B., 2002. Fractured shale-gas systems. Am. Assoc. Pet. Geol. Bull. 86, 1921–1938.

EIA, 2013. Technically recoverable shale oil and shale gas resources. An Assessment of 137 Shale Formations in 41 Countries Outside the United States. U.S. Department of Energy, Washington, DC.

Gasparik, M., Ghanizadeh, A., Bertier, P., Gensterblum, Y., Bouw, S., Krooss, B.M., 2012. High-pressure methane sorption isotherms of black shales from the Netherlands. Energy Fuel 26, 4995–5004.

Gasparik, M., Bertier, P., Gensterblum, Y., Ghanizadeh, A., Krooss, B.M., Littke, R., 2014a. Geological controls on the methane storage capacity in organic-rich shales. Int. J. Coal Geol. 123, 34–51.

Gasparik, M., Rexer, T.F.T., Aplin, A.C., Billemont, P., DeWeireld, G., Gensterblum, Y., Henry, M., Krooss, B.M., Liu, S., Ma, X., Sakurovs, R., Song, Z., Staib, G., Thomas, K.M., Wang, S., Zhang, T., 2014b. First international inter-laboratory comparison of high-pressure CH_4, CO_2 and C_2H_6 sorption isotherms on carbonaceous shales. Int. J. Coal Geol. 132, 131–146.

Gasparik, M., Gensterblum, Y., Ghanizadeh, A., Weniger, P., Krooss, B.M., 2015. High-pressure/high-temperature methane-sorption measurements on carbonaceous shales by the manometric method: experimental and data-evaluation considerations for improved accuracy. SPE J. 20, 790–809.

Gensterblum, Y., van Hemert, P., Billemont, P., Busch, A., Charriére, D., Li, D., Krooss, B.M., de Weireld, G., Prinz, D., Wolf, K.-H.A.A., 2009. European inter-laboratory comparison of high pressure CO_2 sorption isotherms. I: activated carbon. Carbon 47, 2958–2969.

Gensterblum, Y., Merkel, A., Busch, A., Krooss, B.M., 2013. High-pressure CH_4 and CO_2 sorption isotherms as a function of coal maturity and the influence of moisture. Int. J. Coal Geol. 118, 45–57.

Gensterblum, Y., Busch, A., Krooss, B.M., 2014a. Molecular concept and experimental evidence of competitive adsorption of H_2O, CO_2 and CH_4 on organic material. Fuel 115, 581–588.

Gensterblum, Y., Merkel, A., Busch, A., Krooss, B.M., Littke, R., 2014b. Gas saturation and CO_2 enhancement potential of coalbed methane reservoirs as a function of depth. AAPG Bull. 98, 395–420.

Guo, T., Zhang, H., 2014. Formation and enrichment mode of Jiaoshiba shale gas field, Sichuan Basin. Pet. Explor. Dev. 41, 31–40.

Hildenbrand, A., Krooss, B.M., Busch, A., Gaschnitz, R., 2006. Evolution of methane sorption capacity of coal seams as a function of burial history—a case study from the Campine Basin, NE Belgium. Int. J. Coal Geol. 66, 179–203.

Hill, R.J., Zhang, E., Katz, B.J., Tang, Y., 2007. Modeling of gas generation from the Barnett Shale, Fort Worth Basin, Texas. Am. Assoc. Pet. Geol. Bull. 91, 501–521.

Hu, H., Zhang, T., Wiggins-Camacho, J.D., Ellis, G.S., Lewan, M.D., Zhang, X., 2015. Experimental investigation of changes in methane adsorption of bitumen-free Woodford Shale with thermal maturation induced by hydrous pyrolysis. Mar. Pet. Geol. 59, 114–128.

Jarvie, D.M., Hill, R.J., Ruble, T.E., Pollastro, R.M., 2007. Unconventional shale-gas systems: the Mississippian Barnett Shale of north-central Texas as one model for thermogenic shale-gas assessment. Am. Assoc. Pet. Geol. Bull. 91, 475–499.

Ji, L., Zhang, T., Milliken, K.L., Qu, J., Zhang, X., 2012. Experimental investigation of main controls to methane adsorption in clay-rich rocks. Appl. Geochem. 27, 2533–2545.

Ji, W., Song, Y., Jiang, Z., Wang, X., Bai, Y., Xing, J., 2014. Geological controls and estimation algorithms of lacustrine shale gas adsorption capacity: a case study of the Triassic strata in the southeastern Ordos Basin, China. Int. J. Coal Geol. 134–135, 61–73.

Krooss, B.M., van Bergen, F., Gensterblum, Y., Siemons, N., Pagnier, H.J.M., David, P., 2002. High pressure CH_4 and carbon dioxide adsorption on dry and moisture equilibrated Pennsylvanian coals. Int. J. Coal Geol. 51, 69–92.

Long, P., Zhang, J., Jiang, W., Nie, H., Tang, X., Han, S., Xing, Y., 2012. Analysis on pores forming features and its influence factors of reservoir well Yuye-1. J. Cent. South Univ. (Science and Technology) 43, 3954–3963.

Luffel, D.L., Guidry, F.K., 1992. New core analysis methods for measuring rock properties of Devonian shale. J. Pet. Technol. 44, 1184–1190.

Ma, Y., Zhong, N., Li, D., Pan, Z., Cheng, L., Liu, K., 2015. Organic matter/clay mineral intergranular pores in the Lower Cambrian Lujiaping Shale in the north-eastern part of the upper Yangtze area, China: a possible microscopic mechanism for gas preservation. Int. J. Coal Geol. 137, 38–54.

Mahlstedt, N., Horsfield, B., 2012. Metagenetic methane generation in gas shales I. Screening protocols using immature samples. Mar. Pet. Geol. 31, 27–42.

Mavor, M.J., Nelson, C.R., 1997. Coalbed reservoir gas-in-place analysis. Report GRI-97/0263. Gas Research Institute, Chicago, Illinois.

Montgomery, S.L., Jarvie, D.M., Bowker, K.A., Pollastro, R.M., 2005. Mississippian Barnett Shale, Fort Worth Basin, north-central Texas: gas-shale play with multitrillion cubic foot potential. Am. Assoc. Pet. Geol. Bull. 89, 155–175.

Murata, K., El-Merraoui, M., Kaneko, K., 2001. A new determination method of absolute adsorption isotherm of supercritical gases under high pressure with a special relevance to density-functional theory study. J. Chem. Phys. 114, 4196–4205.

Myers, A.L., Monson, P.A., 2002. Adsorption in porous materials at high pressure: theory and experiment. Langmuir 18, 10261–10273.

Pepper, A.S., Dodd, T.A., 1995. Simple kinetic models of petroleum formation. Part II: oil-gas cracking. Mar. Pet. Geol. 12, 321–340.

Rexer, T.F.T., Benham, M.J., Aplin, A.C., Thomas, K.M., 2013. Methane adsorption on shale under simulated geological temperature and pressure conditions. Energy Fuel 27, 3099–3109.

Ross, D.J.K., Bustin, R.M., 2009. The importance of shale composition and pore structure upon gas storage potential of shale gas reservoirs. Mar. Pet. Geol. 26, 916–927.

Sakurovs, R., Day, S., Weir, S., Duffy, G., 2007. Application of a modified Dubinin–Radushkevich equation to adsorption of gases by coals under supercritical conditions. Energy Fuel 21, 992–997.

Schoenherr, J., Littke, R., Urai, J.L., Kukla, P.A., Rawahi, Z., 2007. Polyphase thermal evolution in the infra-Cambrian Ara group (South Oman salt basin) as deduced by maturity of solid reservoir bitumen. Org. Geochem. 38, 1293–1318.

Setzmann, U., Wagner, W., Pruss, A., 1991. A new equation of state and tables of thermodynamic properties for methane covering the range from the melting line to 625 K at pressures up to 1000 MPa. J. Phys. Chem. Ref. Datas 20, 1061–1151.

Sing, K.S., Everett, D.H., Haul, R.A.W., Moscou, L., Pierotti, R.A., Rouquerol, J., Siemieniewsha, T., 1985. Reporting physisorption data for gas/solid systems with special reference to the determination of surface area and porosity. Pure Appl. Chem. 57, 603–619.

Stach, E., Mackowsky, M.-T., Teichmüller, M., Taylor, G.H., Chandra, D., Teichmüller, R., 1982. Stach's Textbook of Coal Petrology. Gebrüder Borntraeger, Stuttgart.

Strąpoć, D., Mastalerz, M., Schimmelmann, A., Drobniak, A., Hasenmueller, N.R., 2010. Geochemical constraints on the origin and volume of gas in the New Albany Shale (Devonian–Mississippian), eastern Illinois Basin. Am. Assoc. Pet. Geol. Bull. 94, 1713–1740.

Tan, J., Weniger, P., Krooss, B.K., Merkel, A., Horsfield, B., Zhang, J., Boreham, C.J., van Graas, G., Tocher, B.A., 2014a. Shale gas potential of the major marine shale formations in the Upper Yangtze Platform, South China, Part II: methane sorption capacity. Fuel 129, 204–218.

Tan, J., Horsfield, B., Fink, R., Krooss, B., Schulz, H.-M., Rybacki, E., Zhang, J., Boreham, C.J., van Graas, G., Tocher, B.A., 2014b. Shale gas potential of the major marine shale formations in the Upper Yangtze Platform, South China, Part III: mineralogical, lithofacial, petrophysical, and rock mechanical properties. Energy Fuel 28, 2322–2342.

Tian, H., Pan, L., Xiao, X.M., Wilkins, R.W.T., Meng, Z.P., Huang, B.J., 2013. A preliminary study on the pore characterization of Lower Silurian black shales in the Chuandong

Thrust Fold Belt, Southwestern China using low pressure N2 adsorption and FE-SEM methods. Mar. Pet. Geol. 48, 8–19.
Tian, H., Pan, L., Zhang, T., Xiao, X., Meng, Z., Huang, B., 2015. Pore characterization of organic-rich Lower Cambrian shales in Qiannan Depression of Guizhou Province, Southwestern China. Mar. Pet. Geol. 62, 28–43.
Wang, S., Song, Z., Cao, T., Song, X., 2013. The methane sorption capacity of Paleozoic shales from the Sichuan Basin, China. Mar. Pet. Geol. 44, 112–119.
Wang, Y., Zhu, Y., Chen, S., Li, W., 2014. Characteristics of the nanoscale pore structure in northwestern Hunan shale gas reservoirs using field emission scanning electron microscopy, high-pressure mercury intrusion, and gas adsorption. Energy Fuel 28, 945–955.
Wei, Z., Wei, X., 2014. Comparison of gas-bearing property between different pore types of shale: a case from the Upper Ordovician Wufeng and Longmaxi Fms in the Jiaoshiba area, Sichuan Basin. Nat. Gas Ind. 34, 37–41 (in Chinese with English abstract).
Weniger, P., Kalkreuth, W., Busch, A., Krooss, B.M., 2010. High-pressure methane and carbon dioxide sorption on coal and shale samples from the Paraná Basin, Brazil. Int. J. Coal Geol. 84, 190–205.
White, C.M., Smith, D.H., Jones, K.L., Goodman, A.L., Jikich, S.A., LaCount, R.B., DuBose, S.B., Ozdemir, E., Morsi, B.I., Schroeder, K.T., 2005. Sequestration of carbon dioxide in coal with enhanced coalbed methane reservoirs—a review. Energy Fuel 19, 659–724.
Xia, X., Chen, J., Braun, R., Tang, Y., 2013. Isotopic reversals with respect to maturity trends due to mixing of primary and secondary products in source rocks. Chem. Geol. 339, 205–212.
Zeng, X.L., Liu, S.G., Huang, W.M., Zhang, C.J., 2012. Comparison of Silurian Longmaxi formation shale of Sichuan Basin in China and carboniferous Barnett Formation shale of Fort Worth Basin in United States. Geol. Bull. China 30, 372–384 (in Chinese with English abstract).
Zhang, T.W., Ellis, G.S., Rupple, S.C., Milliken, K., Yang, R., 2012. Effect of organic matter type and thermal maturity on methane adsorption in shale-gas systems. Org. Geochem. 47, 120–131.
Zou, C., Dong, D., Wang, S., Li, J., Li, X., Wang, Y., Li, D., Cheng, K., 2010. Geological characteristics and resource potential of shale gas in China. Pet. Explor. Dev. 37, 641–653.